Estimating Directional Wave Spectra Properties in Non-Breaking Waves from a UAS-Mounted Multi-beam Lidar

Falk Feddersen[a], Olavo B. Marques[a, b], James H. MacMahan[b], and Robert L. Grenzeback[a]

[a] *Scripps Institution of Oceanography, University of California, San Diego, La Jolla, California*

[b] *Oceanography Department, Naval Postgraduate School, Monterey, California*

Corresponding author: Falk Feddersen, ffeddersen@ucsd.edu

ABSTRACT: Wave spectra and directional moment measurements are of scientific and engineering interest and are routinely measured with wave buoys. Recently both fixed and UAS-mounted lidar remote sensing have measured surfzone wave spectra. However, wave statistics seaward of the surfzone have not been measured with a lidar due to a lower number of returns and directional moments have not been measured at all. We use a multi-beam scanning lidar mounted on a gasoline-powered UAS to estimate wave spectra, slope spectra, and directional moments on the inner shelf in ≈ 10 m water depth from an 11-min hover and compare to a co-located wave buoy. Lidar returns within circular sampling regions with varying radius R are fit to a plane and a 2D parabola, providing sea-surface and slope timeseries. Wave spectra across the sea-swell (0.04–0.4 Hz) are robustly estimated for $R \geq 0.8$ m. Estimating slope spectra is more challenging. Large R works well in the swell band and smaller R work well at higher frequencies, comparing well with a wave buoy inferred slope spectra. Directional Fourier coefficients are estimated from wave and slope spectra and cross-spectra and are compared to a wave buoy in the sea-swell band. Larger R and the 2D parabola-fit yield better comparison to the wave buoy. Mean wave angles and directional spreads, functions of the directional Fourier coefficients, are well reproduced at $R = 2.4$ m and the 2D-parabola fit, within the uncertainties of the wave buoy. This UAS-mounted multi-beam scanning lidar and this methodology can be used in regions where wave buoys are not easily deployable, e.g., near rocky coasts or cliffs.

SIGNIFICANCE STATEMENT: Previously fixed or hovering lidar have been used to estimate wave spectra in the surf and swash zone where lidar returns are high due to the reflectance of foam. We present methodology to accurately estimate wave spectra and directional properties on the inner-shelf where waves are not breaking using a hovering Uncrewed Aircraft System with a mounted lidar. The estimated wave spectra and directional statistics compare well with a Spotter wave buoy demonstrating the methods robustness.

1. Introduction

Measurements of surface gravity wave statistics are required for both scientific research and engineering applications. Wave statistics of interest are the frequency-dependent sea-surface (η) elevation spectra $S_\eta(f)$, from which significant wave height H_s, peak and mean periods are based, as well as directional moments such as mean wave angle $\theta(f)$ and directional spread $\sigma_\theta(f)$ (Kuik et al. 1988). These directional moments are derived from the first four Fourier coefficients of the directional spectra and are denoted $a_1(f)$, $b_1(f)$, $a_2(f)$, and $b_2(f)$ (Longuet-Higgins et al. 1963). Wave spectra and directional moments are typically derived from pitch-and-roll wave buoys (e.g., Kuik et al. 1988), co-located pressure sensor and current meter (e.g., Herbers et al. 1999), or from Acoustic Doppler Current Profilers (ADCP, e.g., Herbers and Lentz 2010), using spectra and cross-spectra of measured variables. More recently, attention has been focused on the development of inexpensive wave buoys that are either GPS-based (e.g., Herbers et al. 2012; Raghukumar et al. 2019) or inertial measurement unit (IMU) based (e.g., Rabault et al. 2022; Feddersen et al. 2023a).

Lidar (light detection and ranging) is a remote sensing tool with significant potential for studying surface gravity waves as a lidar return is a direct measure of the distance to the water surface. An aircraft-mounted scanning (rotating 360°) single-beam lidar measured the sea surface near a wave buoy, and aircraft-lidar derived and buoy derived (non-directional) wave spectra compared well (Hwang et al. 2000). Since then, aircraft-based lidar wave measurements have advanced significantly (e.g., Melville et al. 2016) and can resolve to the high wavenumber portion of the wave spectrum (Lenain and Melville 2017). However, as a single scanning beam is used, two-dimensional (2D) statistical observations are obtained by assuming a statistically spatially homogeneous wave field. Such assumptions cannot be made in coastal regions where the waves are transforming.

Fixed-location lidar-based temporal sea-surface elevation measurements were first performed by Irish et al. (2006). They mounted four non-scanning point-beam lidars in a rectangular grid with horizontal spacing of 0.6–2.0 m on the Field Research Facility (FRF, North Carolina USA) pier 6–16 m above the water surface. Wave spectra $S_\eta(f)$ and significant wave heights were well reproduced, but the array spacing and instrument number were not ideal for estimating directional moments. Single-beam scanning lidars mounted on a fixed location have been used to measure the temporal (t) and cross-shore (x) varying sea-surface $\eta(x,t)$ in the swashzone on sandy (Blenkinsopp et al. 2010) and gravel (Almeida et al. 2013) beaches. Blenkinsopp et al. (2010) showed that swash zone η estimated from a 905 nm wavelength lidar, matched well with ultrasonic altimeters deployed in the swash zone. Using a fixed scanning lidar at a 1550 nm wavelength, Brodie et al. (2015) showed that lidar-derived wave setup and wave spectra matched those of pressure sensors in the inner-surfzone at low grazing angles and distances 25–65 m from the lidar. A fixed 1550 nm lidar scanning a highly-energetic, low-sloped beach compared well to a swash zone pressure sensor at ranges of 250-350 m also at low grazing angles (Fiedler et al. 2015). Three fixed lidars mounted on a pier were used to generate a cross-shore continuous timeseries of sea surface elevation across the surfzone (Martins et al. 2017). As these studies used a single-beam scanning lidar, only a single spatial direction was resolved, and directional wave information could not be estimated.

The aerated nature of water in the swash and surf zone is ideal for lidar reflections at all wavelengths. For non-breaking waves, lidar returns depend on the lidar wavelength. Lidars with wavelength near 900 nm perform far better on water surfaces than lidars at 1550 nm due to the order of magnitude smaller absorption coefficient at 905 nm (Wojtanowski et al. 2014). Thus, lidar at a 1550 nm wavelength is more limited in measuring waves seaward of the surfzone where the water surface is not aerated. A lidar with a 905 nm wavelength was able to well reproduce wavestaff-based wave observations in a laboratory (Blenkinsopp et al. 2012). Detailed observations of wave overturning have been made using a multi-beam 905 nm scanning lidar in both field settings (O'Dea et al. 2021) and field-scale laboratory settings (Feddersen et al. 2023b; Baker et al. 2023).

An uncrewed aircraft system (UAS) with RTK-GNSS positioning and video were used to study beach profile evolution with structure from motion (Turner et al. 2016), and observe the wave speed to estimate bathymetry (Brodie et al. 2019; Lange et al. 2023). As a more direct measurement, lidar has advantages and liabilities over video. UAS with a mounted lidar is used in various mapping and surveying applications that were enabled by advances in UAS, positioning (GPS & IMU), and lidar technology. One advantage of a UAS with mounted lidar is the high grazing angles, which are more conducive to returns than the low grazing angles of shore-mounted systems. Surface gravity waves and tides were estimated at a single location by an 870 nm scanning lidar at a height 6-10 m above the surface and were validated against an in situ pressure gauge (Huang et al. 2018). Fiedler et al. (2021) extended this work with a 905 nm scanning lidar mounted on a UAS. Wave spectra within the surfzone and swash zone were estimated and validated against in situ pressure sensor data. However, observations were limited seaward of the surfzone where wave breaking did not occur, and no directional information was estimated.

In contrast to single-beam scanning lidars, multi-beam scanning lidars enable two-dimensional (2D) sea-surface elevation measurements, allowing for directional wave analysis with a single instrument. Here, we use a gasoline-powered UAS with a multi-beam 903 nm wavelength scanning lidar payload to estimate directional wave statistics at a location seaward of the surfzone in 10 m water depth and compare to a Spotter wave buoy. The UAS together with the lidar package, as well as the data collection by the co-located Spotter buoy are described in Section 2. Binning regions of different radii are defined, and the statistics of lidar returns, as well as the method for fitting the sea surface and its slope are described in Section 3. In Section 4, UAS-lidar estimated timeseries of η and $\partial\eta/\partial x$, bulk statistics, as well as S_η and slope spectra $S_{|\nabla\eta|}$ are examined as a function of the radius of the binning-region. UAS wave spectra are compared to that of the Spotter wave buoy. UAS slope spectra are compared to slope spectra estimated from Spotter wave spectra and the wavenumber k inferred from the linear dispersion relationship. In Section 5, UAS-lidar estimated directional Fourier coefficients are estimated as a function of frequency and compared to those of the Spotter wave buoy. Directional moments derived from the Fourier coefficients are also compared to the Spotter wave buoy. The capability of a UAS with multi-beam lidar to estimate wave and slope spectra as well as directional wave quantities is discussed in Section 6.

2. Methods

a. Experiment Overview

The ROXSI field experiment (Marques et al. 2023) occurred during July 2022 off of China Rock on the Monterey Peninsula, CA USA (Fig. 1). The rocky shore off of China Rock has a moderate

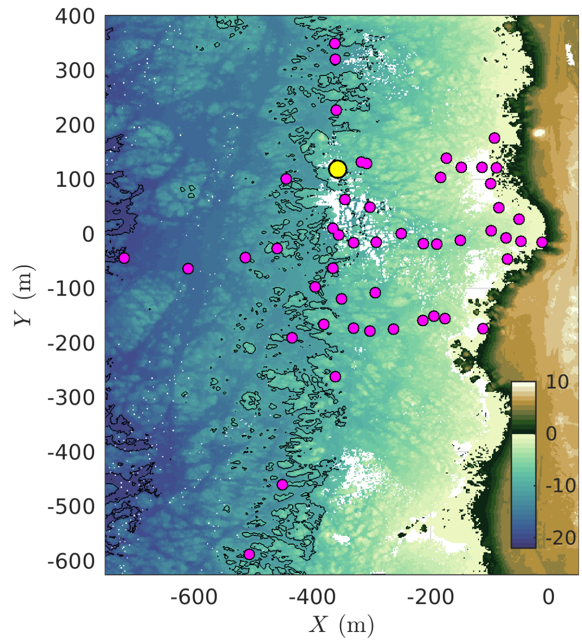

FIG. 1. Bathymetry (z in mean sea-level) as a function of local cross-shore (X) and alongshore (Y) coordinates. Magenta dots represent all instrument locations. The yellow circle represents the location of the Spotter mooring where the hover took place. Regions in white indicate no bathymetry observations.

(1:40) cross-shore slope. In water depths $h < 20$ m, the bathymetry has significant variability, or roughness, at a range of length-scales (Fig. 1). A China Rock cross- and alongshore (X,Y) coordinate system is defined where $-X$ is directed towards 285° N. The shoreline has multiple small headlands about 250 m apart with embayments that extend 100 m onshore. During the experiment a number of instruments, including ADCPs, Spotter wave buoys (Raghukumar et al. 2019), and pressure sensors were deployed from the shoreline to 30 m water depth (blue dots in Fig. 1). At 8 locations, co-located Spotter wave buoys and time-synchronized pressure sensors were deployed (Marques et al. 2023). Spotter wave buoys are GPS-based (Herbers et al. 2012), and are highly effective in capturing wave spectra $S_\eta(f)$ and directional moments in the sea-swell ($0.05 < f < 0.3$ Hz) frequency band (e.g., Raghukumar et al. 2019; Collins et al. 2023). To estimate directional parameters, wave buoys (whether GPS- or IMU-based) use displacement or slope cross-spectra to estimate the Fourier coefficients of the directional spectra (or directional Fourier coefficients) $a_1(f)$, $a_2(f)$, $b_1(f)$, and $b_2(f)$ (Longuet-Higgins et al. 1963; Kuik et al. 1988). Although only tested out to 0.3 Hz (Raghukumar et al. 2019; Collins et al. 2023), the Spotter wave buoy reports spectral quantities out to 1 Hz with unknown accuracy from 0.3–1 Hz.

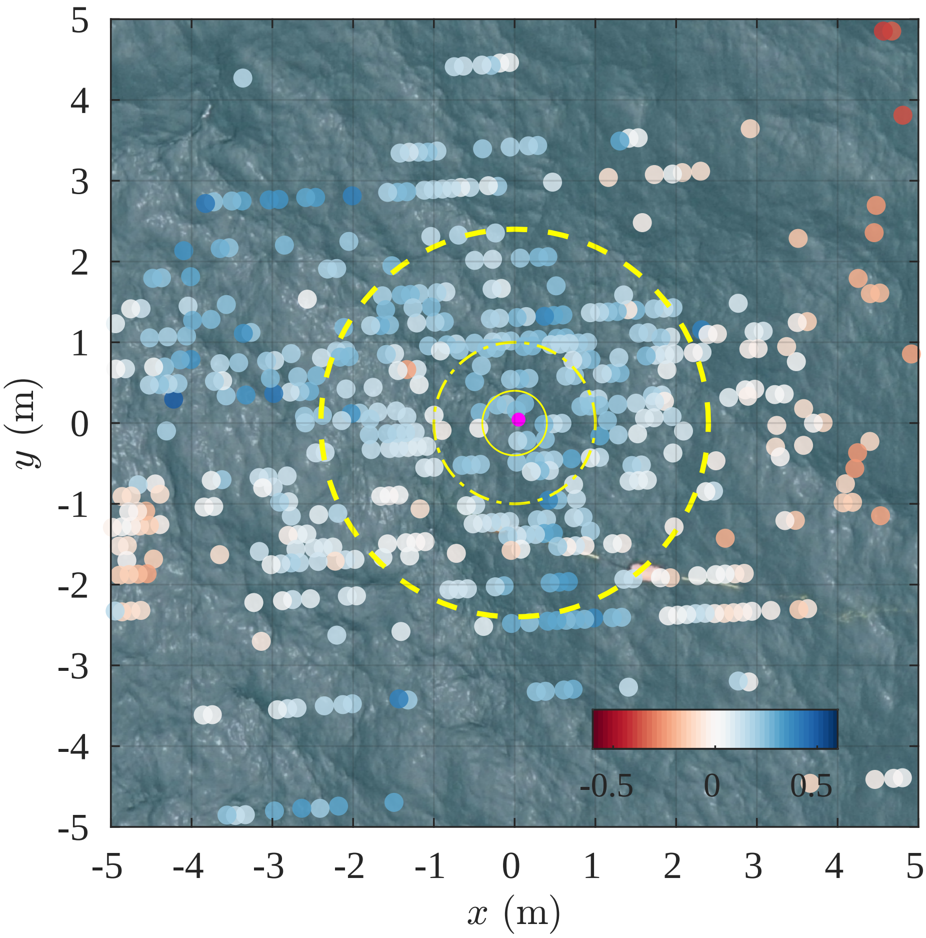

FIG. 2. Georectified sea-surface image in offset China Rock (x, y) coordinates with overlaid lidar-based sea-surface elevation $\eta(x, y)$ (dots). Lidar returns are at 10 Hz. The magenta dot indicates the UAS location. The solid, dash-dot, and dashed yellow circles represent radii of $R = \{0.4, 1, 2.4\}$ m around $(x, y) = (0, 0)$ m. The time is 19-July-2022 14:59:08 PDT.

b. UAS and Lidar-Package Description

We use an eight-rotor Skyfront Perimeter 8 as the Uncrewed Aircraft System (UAS). The Perimeter 8 is powered by a hybrid gasoline-electric propulsion system, consisting of a 32 cc 1-cylinder 2-stroke engine that generates electricity to power the UAS. Two Lithium Polymer (LiPo) batteries provide startup and emergency backup power. Tip-to-tip, the Perimeter 8 measures 2.31 m long by 2.2 m wide by 0.37 m high. The Perimeter 8 weighs ≈ 20 kg with 4 L of fuel and the payload gives it a takeoff weight of ≈ 22.5 kg. Fully loaded, the UAS was flown for up to 100 min, including takeoff, kinematic alignment maneuvers, transit, hovers, and landing. The Skyfront Perimeter 8 uses a proprietary PX4-based flight controller and is remotely operated using a 2.4 GHz radio remote controller connected to a Windows laptop running the Skyfront Ground Control Software (GCS) for both manual and automated waypoint flight. The flight controller navigation system was upgraded with a RTK-GNSS module that receives relative position updates from a fixed base station on shore. This allows the UAS to maintain its position without drifting over time. With a team of three people, the lidar UAS can be set up and deployed within 30 min of arrival on site. The downtime between each flight to refuel, swap batteries, and resume data collection was approximately 20 minutes. External LiPo batteries are used for ground power to keep the lidar and GNSS system running without interruption.

The UAS payload is a Phoenix Lidar Systems (PLS) Scout-Ultra, consisting of a Velodyne Ultra Puck (VLP-32C) lidar, a proprietary PLS NavBox, and a 24 MP Sony A6K-Lite RGB camera. The Scout-Ultra NavBox integrates the inertial measurement unit (IMU), GNSS receiver, data storage, CPU, Wi-Fi telemetry, power supply, and I/O components necessary for collecting survey-grade data. The GNSS receiver is a Novatel OEM7720 and the IMU is an Inertial Labs IMU-P. Dual helical GNSS antennas are mounted onto opposing UAS motor arms with 1.54 m separation, enabling accurate heading solutions. The IMU and dual GNSS data are post-processed using Novatel Inertial Explorer Version 8.90 software to produce a trajectory file for determining sensor position and orientation. The Scout-Ultra is controlled separately from the UAS via a Wi-Fi link to a second Windows laptop running PLS Spatial Explorer version 6.0.7. The PLS software displays real-time point cloud, image preview, and payload telemetry data, and allows for remote activation of the lidar and camera sensors. RGB camera images were taken at 1 Hz.

The Velodyne Ultra Puck lidar was originally developed for the automobile industry and has been adapted for surveying and robotics applications. Although it is slightly less accurate than fixed lidars previously used in surfzone studies, its low cost, low power, multi-beam scan pattern, long-range, small form factor, and light (1 kg) weight make it well-suited for this UAS application. The lidar uses a 903 nm laser, which performs better on water surfaces than 1550 nm lasers (Wojtanowski et al. 2014; Fiedler et al. 2021). The 32 beams scan over 360°, on an axis 90° from the nose of the UAS. The beams are organized in a non-linear distribution, with most beams concentrated in the center of the vertical field of view, where data resolution is increased, resulting in a 40° off-axis field of view (-25° deg to +15°). The pulse repetition rate of the sensor is 600,000 measurements per second (600 kHz). The programmable frame rate of the instrument ranges from 5 to 20 Hz. Similar to Feddersen et al. (2023b), we used 10 Hz (600 RPM, ±3 RPM), which gives a horizontal angular (azimuthal) resolution of 0.2°. The maximum measurement range is 200 m with a ±3 cm range accuracy. Laser beam divergence is 3.43 mrad on the horizontal axis (crossshore) and 1.72 mrad on the vertical axis (alongshore), resulting in a 12.5 cm × 6.6 cm laser footprint directly below the scanner when hovering at 33 m above the sea surface. The lidar returns are transformed into earth coordinates in Spatial Explorer software using the post-processed position and orientation data. The resulting point cloud was exported to a LAS format file. Lidar returns were quality controlled to remove points closer than 8 m or farther than 100 m from the lidar.

c. Hover near the Spotter Wave Buoy

Most missions had the UAS hovering over locations of pressure sensors for approximately 10 min at a time. However, we performed one mission where the UAS hovered near the location of a Spotter wave buoy (Fig. 1, yellow circle), approximately 250 m from the mean shoreline. This hover occurred on 19-July-2022, started at 14:58:12 PDT, and lasted for 692 seconds. At this time, the Spotter significant wave height integrated from 0.04–0.5 Hz was $H_\mathrm{s} = 1.16$ m with an energy-weighted mean period of $T_\mathrm{mean} = 5.6$ s. During the morning the wind (measured 300 m offshore at 4 m above the sea-surface) had been 6 $\mathrm{m\,s^{-1}}$ blowing onshore ($+x$ direction). However, during the hover, the wind was weaker at 2.5 $\mathrm{m\,s^{-1}}$ onshore. The UAS was hovering at 33 m elevation relative to the sea surface where the wind was likely stronger than measured.

The hovering UAS was oriented with the nose pointing in the alongshore $+Y$ direction so the scanner was oriented for cross-shore scanning. The latitude and longitude of lidar returns are converted to the UTM-based local China Rock (X,Y) coordinates. The vertical locations of the lidar returns are in NAVD88 and are demeaned to represent sea-surface elevation. The 2-Hz sampled locations of the UAS reveal that the UAS maintained a constant hovering position. The position x standard deviation $\sigma_x = 0.055$ m is small as is the y-standard deviation $\sigma_y = 0.084$ m, with maximum position deviation < 0.2 m in x and y. During the hover, the UAS held its orientation consistently with a heading standard deviation of 0.3°, pitch standard deviation of 0.7° and roll standard deviation of 0.5°. The mean roll was 2.7° allowing the UAS to maintain position in the wind.

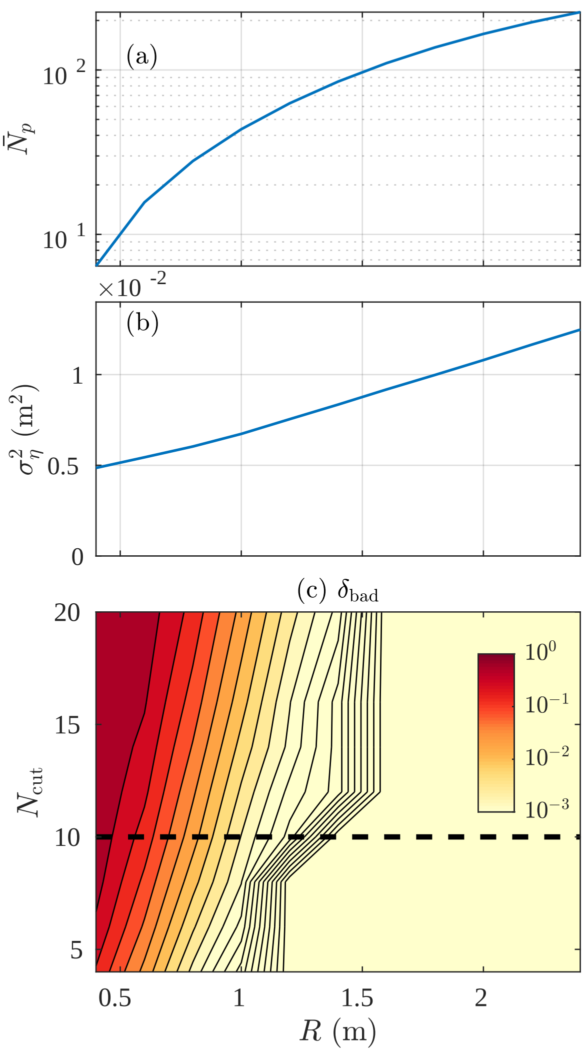

FIG. 3. Lidar return statistics within the sample region versus radius R: (a) the time-averaged number of returns within the sample region $\bar{N}_p$ (b) the mean variance of the sea surface returns within the sample region σ_η^2 (1). (c) the fraction of time δ_{bad} as a function of the return cutoff number N_{c} and the radius R. The black dashed line represents $N_{\mathrm{c}} = 10$.

An example of a single 10 Hz lidar snapshot is shown in Fig. 2. We define a local coordinate system $x = X - \bar{X}$ where $(\bar{X}, \bar{Y})$ are the mean location of the UAS during the hover. From the georectified image, a rough but not whitecapping sea surface is visible with short wavelengths ≈ 1 m that ride on top of the longer sea and swell. The Velodyne Ultra lidar beams are largely oriented along the $\pm x$ direction and lidar returns are largely concentrated at $|y| \leq 2$ m. The number of lidar returns at this offshore location was less than farther onshore due to the increased water clarity at this cross-shore location (divers reported 6 m visibility 2 days later). Lidar returns indicate that the sea surface η varies spatially at ± 0.5 m at a range of scales.

3. Lidar Data Processing and Return Statistics

We define a *sampling region* as a circle of radius R centered on the mean hover location $(x, y) = (0, 0)$ m. A circle is chosen so as to not bias directional estimates, i.e., all directions have the same sampling region width. We estimate lidar return statistics and sea-surface elevation and slopes as a function of R, which varies from 0.4 m to 2.4 m in 0.2 m increments. An example of sampling regions are shown in Fig. 2 with radii of $R = \{0.4, 1, 2.4\}$ m. The number of lidar returns within a sampling region, defined as $N_p(t; R)$, is higher for larger R (Fig. 2). We define two types of averaging. The first is averaging over the lidar returns within the sample region, denoted by $\langle \ldots \rangle$. The second is a time-average over the 692 s of the UAS hover, denoted by an overbar.

The time-averaged number of lidar returns $\bar{N}_p(R)$ varies from 6 points for $R = 0.4$ m and increases quadratically to $\bar{N}_p = 225$ for $R = 2.4$ m (Fig. 3a). The ratio $\bar{N}_p/R^2$ is roughly constant at ≈ 40, indicating that the lidar return density is uniform across this range of R. At larger R, this ratio decreases due to the lidar beam distribution, and larger R are thus not considered.

We estimate the time-average vertical variance of lidar returns within a sample region, $\sigma_\eta^2(R)$, as

$$\sigma_\eta^2(R) = \overline{\langle \eta'^2 \rangle}, \tag{1}$$

where $\eta_i'(t) = \eta_i(t) - \langle \eta(t) \rangle$. Thus, σ_η^2 represents a combination of instrument noise and the true sea-surface variability. The mean return vertical variance $\sigma_\eta^2(R)$ varies in a weakly quadratically manner from from 0.005 m^2 at $R = 0.4$ m to 0.013 m^2 at $R = 2.4$ m (Fig. 3b). Quadratic σ_η^2 variation is consistent with the sea surface primarily being a plane, whereas random and independent instrument noise would lead to a $\sigma_\eta^2(R)$ constant with R. Extrapolating the curve to $R = 0$, yields an instrument (lidar plus orientation/position) noise estimate of 0.0035 m^2 or 0.06 m. The quoted Velodyne Ultra Puck accuracy is 0.03 m, or half of the inferred noise standard deviation, suggesting the remainder is due to UAS orientation and position uncertainty.

For a particular time, a minimum number of lidar returns above a cutoff N_c are required, (i.e., $N_p(t) > N_\mathrm{c}$) to ensure confidence in data quality and robust sea-surface statistics. We examine cutoffs that vary from $N_\mathrm{c} = 4$ to $N_\mathrm{c} = 20$. We define $\delta_\mathrm{bad}(R, N_\mathrm{c})$ as the fraction of time that $N_p(t;R) < N_c$. Small δ_{bad} results in minimal timeseries interpolation prior to estimating wave statistics. Yet small N_c may lead to noisy estimates of η and its slope. We examine the statistics of δ_{bad} as a function of R and N_c. For $R > 1.2$ m, the fraction of bad data $\delta_{bad}(R,N_c)$ is largely independent of N_c (contour lines in Fig. 3c are largely vertical) and $\delta_{bad} < 10^{-3}$ for all N_c, indicating minimum timeseries interpolation requirement at these R. For smaller $R \leq 0.6$ m, δ_{bad} also increases strongly with N_c and even for $N_c = 4$ is always > 0.05. Because of their large δ_{bad}, we do not consider further $R \leq 0.6$ m. As δ_{bad} only weakly depends on N_c for $R \geq 0.8$ m, we choose a intermediate $N_c = 10$ for further analysis.

To calculate wave spectra and directional moments, timeseries of η, $\partial\eta/\partial x$, and $\partial\eta/\partial y$ are required. At each time where $N_c \geq 10$, we estimate these parameters for the range R using two different least-squares fits: (1) a plane-fit and (2) a 2D parabola-fit. The plane-fit fits a plane to the available lidar returns in the sampling region, i.e.,

$$\eta_i(t,x_i,y_i) = \frac{\partial\eta}{\partial x}(t)x_i + \frac{\partial\eta}{\partial y}(t)y_i + \eta(t), \tag{2}$$

where (x_i, y_i) and η_i are the observed horizontal position and sea-surface elevation of the lidar returns (Fig. 2), and there are three fit parameters (η, $\partial\eta/\partial x$, and $\partial\eta/\partial y$). The 2D parabola-fit fits to a 2D parabola, i.e.,

$$\eta_i(t,x_i,y_i) = \frac{1}{2}\frac{\partial^2\eta}{\partial x^2}(t)x_i^2 + \frac{1}{2}\frac{\partial^2\eta}{\partial y^2}(t)y_i^2 + \frac{\partial^2\eta}{\partial y\partial x}(t)x_iy_i + \frac{\partial\eta}{\partial x}(t)x_i + \frac{\partial\eta}{\partial y}(t)y_i + \eta(t), \tag{3}$$

and has three additional fit parameters $\partial^2\eta/\partial x^2$, $\partial^2\eta/\partial y^2$, and $\partial^2\eta/\partial x\partial y$. Any times with $N_p < N_c$ lidar returns are linearly interpolated in time. The advantage of the plane-fit (2) is that with fewer fit parameters, their estimates should be more stable. The disadvantage is that, for a wavelength λ, an R significantly shorter than λ is required to resolve the wave. This places an upper frequency limit, through the surface gravity wave dispersion relationship (A1), on the estimated parameters. As λ gets smaller (frequency increases), we expect the spectral levels to decrease with larger R, as the fit essentially acts as a low-pass filter. The 2D parabola-fit (3) has more fit-parameters, which will have more noise than that of the plane-fit. However, by including quadratic terms at a fixed R, a shorter λ should be resolvable relative to the plane-fit, thereby increasing the resolved frequencies. Throughout, we will explore the relative merits of both fit methods. At larger λ, other challenges

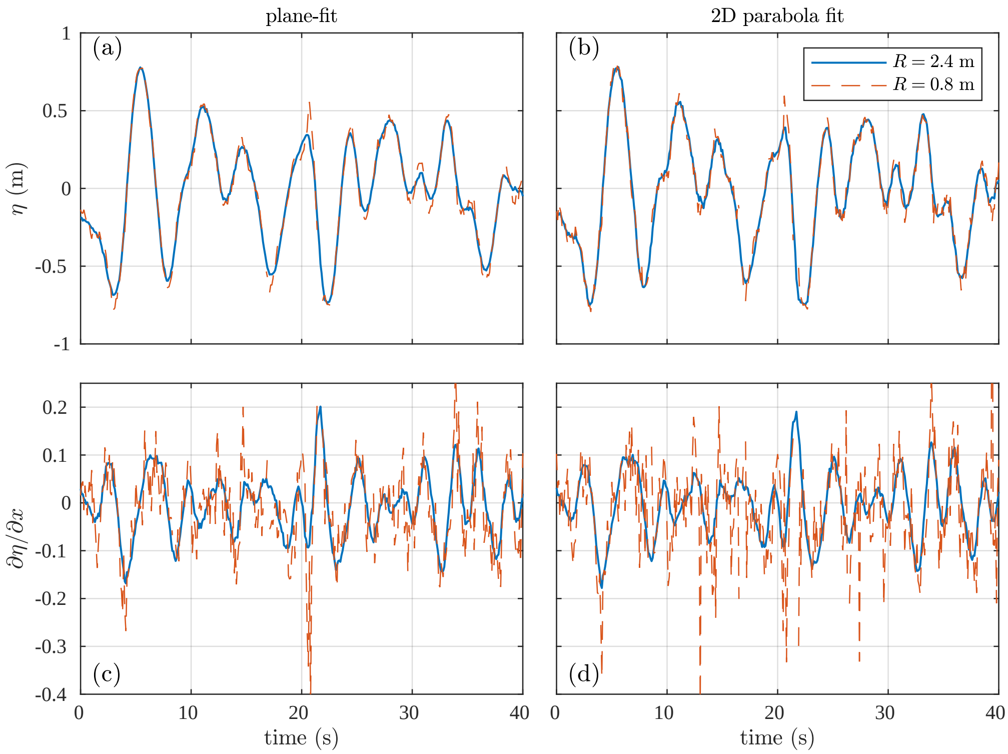

FIG. 4. Timeseries of (top, a-b) η and (bottom, c-d) $\partial\eta/\partial x$ for $R = 2.4$ m (blue) and $R = 0.8$ m (orange-dashed) and $N_c = 10$. The left column (a,c) is for the plane-fit and the right column (b,d) is for the 2D parabola-fit.

are present that depend on R. The wave slope scales as wave amplitude over wavelength a/λ, and thus these smaller slopes will be harder to robustly estimate.

4. Lidar Observations of Sea Surface and Slope

a. Timeseries of η and $\partial\eta/\partial x$

Short, 40-s, timeseries of the plane-fit and 2D parabola-fit η and $\partial\eta/\partial x$ for two radii are shown in Fig. 4 to illustrate the effects of varying R and the fit method. Recall $N_c = 10$ is fixed. The plane-fit η with $R = 2.4$ m varies ± 0.5 m with evident variability over 3–8 s periods (Fig. 4a, blue curve). The $R = 0.8$ m plane-fit η varies similarly but has more high-frequency variability (orange-dashed in Fig. 4a). The 2D parabola-fit η for $R = 2.4$ m (Fig. 4b, blue curve) is quite similar to that of the plane-fit, and the η for $R = 0.8$ m also has more high-frequency variability with some minor differences relative to the plane-fit η. The differences in $\partial\eta/\partial x$ for the two radii are much starker (Fig. 4c,d) than for η. The plane-fit $\partial\eta/\partial x$ for $R = 2.4$ m has a smooth curve (Fig. 4c) with variability at time-scales similar to η with magnitude ≈ 0.1, indicating weak nonlinearity. However, the $R = 0.8$ m plane-fit η has significantly more high-frequency variability than for $R = 2.4$ m. The 2D parabola-fit $\partial\eta/\partial x$ for $R = 2.4$ m (blue curve in Fig. 4d) is similar to the plane-fit. However, the $R = 0.8$ m $\partial\eta/\partial x$ has even more high-frequency variability than for the plane-fit. For both η and $\partial\eta/\partial x$, the greater stability and low-pass filtering effect of increasing R is evident. The pattern with $\partial\eta/\partial y$ is similar (not shown).

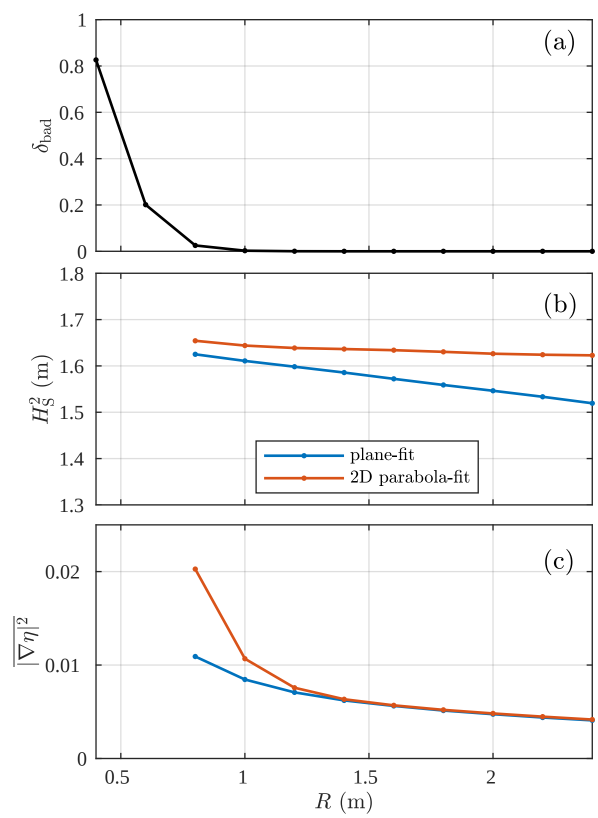

Fig. 5. (a) Fraction of time with bad data δ_{bad} (b) squared significant wave height H_s^2 (4), and (c) mean square surface slope $\overline{|\nabla\eta|^2}$ (5) versus radius R all for $N_c = 10$. In panels (b)-(c), the blue and orange lines represent the plane-fit and 2D parabola-fit, respectively.

b. Time-averaged sea-surface and slope statistics

To evaluate the η, $\partial\eta/\partial x$, and $\partial\eta/\partial y$ from the two fit methods, we examine three bulk statistics, squared significant wave height H_s^2 and mean square wave slope as a function of R. Significant wave height H_s is defined in a standard manner through sea-surface elevation variance,

$$H_\mathrm{s} = 4\overline{\eta^2}^{1/2}. \tag{4}$$

Note, this definition includes all frequencies up to the Nyquist frequency of 5 Hz in the estimate of H_s. The mean-square wave slope $\overline{|\nabla\eta|^2}$ is

$$\overline{\left(\frac{\partial\eta}{\partial x}\right)^2 + \left(\frac{\partial\eta}{\partial y}\right)^2}. \tag{5}$$

For $R = 0.4$ m and $R = 0.6$ m, $\delta_\mathrm{bad} = 0.83$ and $\delta_\mathrm{bad} = 0.2$, respectively (Fig. 5a). With so many bad data points, further statistics are not calculated or examined for $R \le 0.6$ m. For $R = 0.8$ m, $\delta_\mathrm{bad} = 0.03$, and for larger R the δ_bad is effectively zero. Thus, we examine statistics for $R \ge 0.8$ m only. The plane-fit H_s^2 slowly decreases from 1.63 m^2 at $R = 0.8$ m to 1.52 m^2 at $R = 2.4$ m (Fig. 5b). This decrease is consistent with the larger R, providing more statistical stability and acting as a low-pass filter. Relative to the plane-fit, the 2D parabola-fit H_s^2 is relatively constant with R only decreasing slightly from 1.65 m^2 to 1.62 m^2 over the R range. This indicates that for this R range the 2D parabola-fit with its extra fit parameters reduces the low-pass filter effect. For the plane-fit, the mean square slope $\overline{|\nabla\eta|^2}$ decreases steadily from 0.011 at $R = 0.8$ m to 0.0041 at $R = 2.4$ m (fig. 5c). For the 2D parabola fit, $\overline{|\nabla\eta|^2}$ is twice as large as for the plane fit for $R = 0.8$, consistent with the $\partial\eta/\partial x$ timeseries (Fig. 4d). However, for $R \ge 1.2$ m, the 2D parabola-fit $\overline{|\nabla\eta|^2}$ is similar to that of the plane-fit method (Fig. 5c). The decay with R suggests that slope is more sensitive to R than η is for the 2D parabola-fit method.

c. Spectra of sea-surface elevation and slope

Sea-surface elevation spectra $S_\eta(f)$ are estimated for both fit-methods with 24 degrees-of-freedom (DOF) and frequency resolution of ≈ 0.01 Hz. Slope spectra $S_{|\nabla\eta|}(f)$ are also estimated from the spectra of $\partial\eta/\partial x$ and $\partial\eta/\partial y$,

$$S_{|\nabla\eta|}(f) = S_{\eta_x}(f) + S_{\eta_y}(f). \tag{6}$$

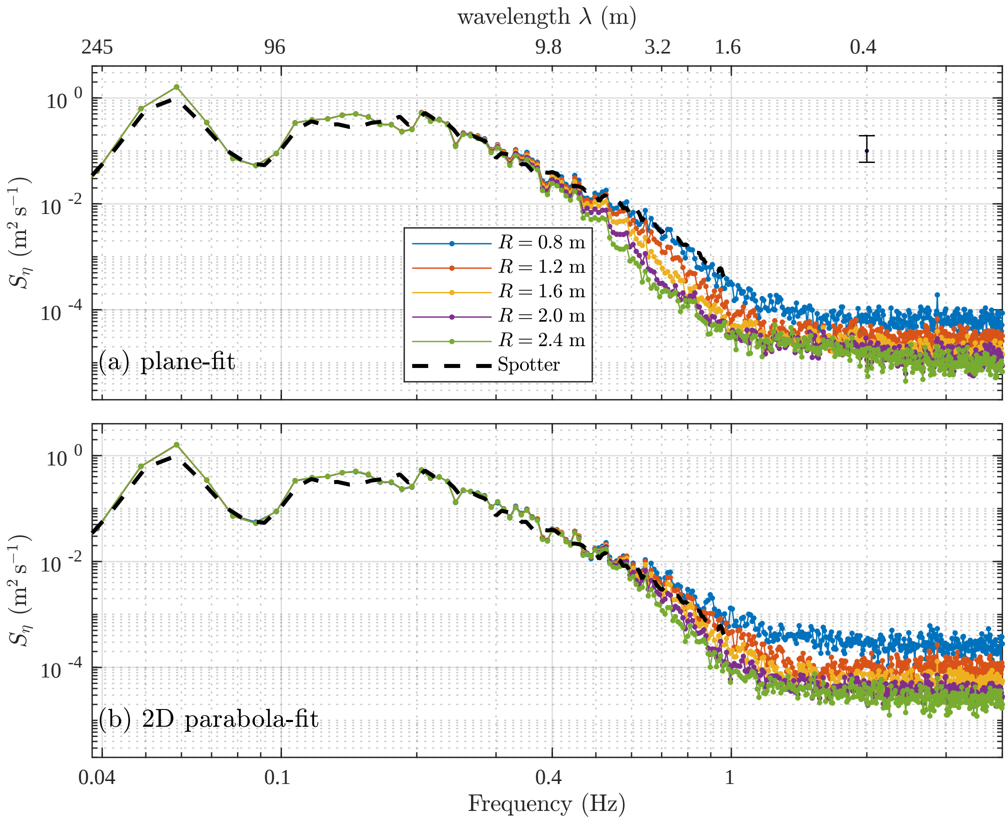

FIG. 6. Sea-surface elevation spectra $S_\eta(f)$ versus frequency for the (a) plane-fit and (b) 2D parabola-fit methods for $R = \{0.8, 1.2, 1.6, 2.0, 2.4\}$ m. The black dashed curve is the Spotter wave buoy spectrum at the same time (shown out to 1 Hz). The black error bar indicates the 95% spectra confidence limits at 24 DOF. On the top is shown the wavelength λ associated with select f through the linear surface gravity wave dispersion relationship (A1) at a depth of 10 m.

We examine wave spectra $S_\eta(f)$ dependence on radius R for both fit-methods and compare it to the wave spectra from the co-located Spotter wave buoy (Fig. 6). Hereafter, we define three specific frequency bands. First, the swell band spans $0.04 \leq f < 0.1$ Hz. The sea band spans $0.1 \leq f < 0.4$ Hz. We also define a "chop" band as $0.4 \leq f < 1$ Hz band. The plane-fit $S_\eta(f)$ for $R \geq 0.8$ m match well the Spotter wave spectra across the $0.04 < f < 0.4$ Hz band that encompasses the swell and sea bands. In this band, the plane-fit and 2D-parabola fit $S_\eta(f)$ are nearly similar for all $R \geq 0.8$ m. At this depth, a frequency of 0.4 Hz corresponds to a wavelength of ≈ 10 m, more than four times larger than the largest R. At frequencies > 0.4 Hz, $S_\eta(f)$ decreases more rapidly for larger R, consistent with the low-pass filter effect with larger R, and at 0.6 Hz significant $S_\eta(f)$

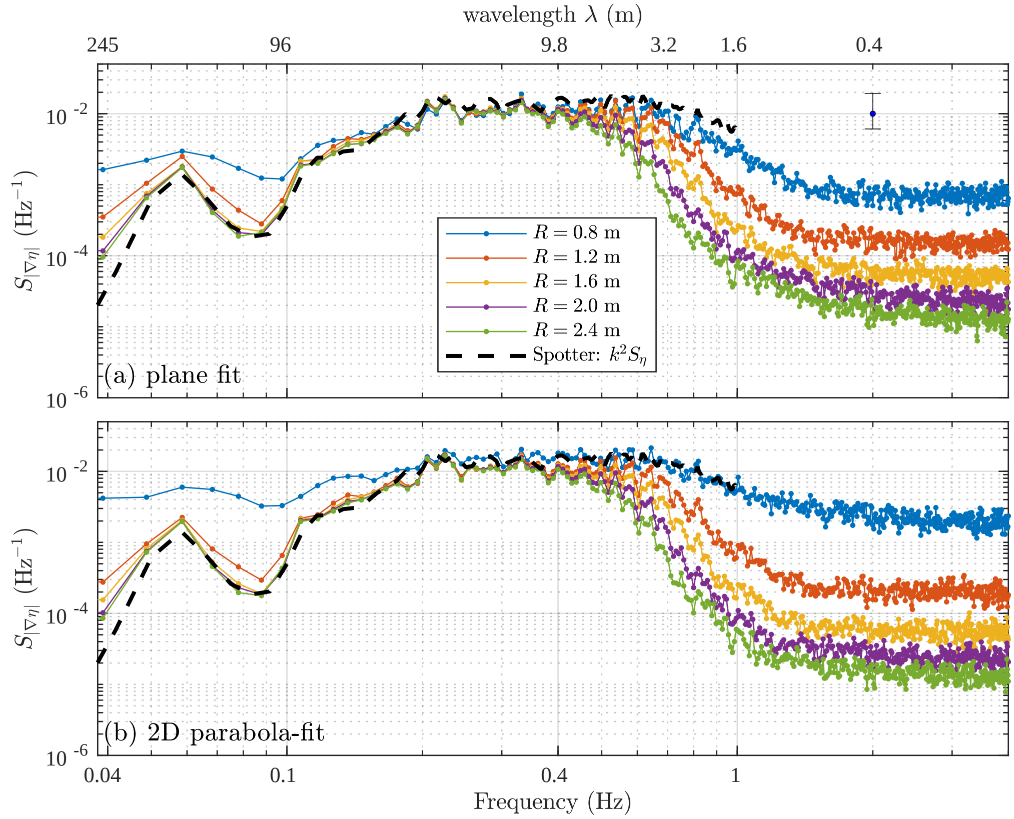

FIG. 7. Sea-surface elevation slope spectra $S_{|\nabla\eta|}$ (6) versus frequency for the (a) plane-fits and (b) 2D parabola-fit methods for $R = \{0.8, 1.2, 1.6, 2.0, 2.4\}$ m. The black dashed curve is the Spotter estimated slope spectrum $k^2 S_\eta(f)$ using the dispersion relationship (A1) and a depth of 10 m. The black error bar indicates the 95% spectra confidence limits at 24 DOF. On the top is shown the wavelength λ associated with select f through the linear surface gravity wave dispersion relationship at a depth of 10 m.

differences with R are evident, particularly for the plane-fit (Fig. 6). The 2D parabola-fit $S_\eta(f)$ has less spectral variation with R in the "chop" (0.4–1 Hz) band then the plane-fit, consistent with the H_s^2 changes with R for both methods (Fig. 5b). This is likely a result of the 2D parabola-fit being able to resolve shorter wavelengths at a particular R. For both methods, the spectral noise floor (i.e., flat $S_\eta(f)$) occurs at $f > 1$ Hz, corresponding to a wavelength of 1.6 m, with levels that decrease with R. Thus, either method will work well for estimating wave spectra in the sea-swell (0.04–0.4 Hz) band.

We next examine the effect of R on slope spectra $S_{|\nabla\eta|}(f)$ (6) for both the plane-fit and 2D parabola-fit methods (Fig. 7). The Spotter does not report wave slope, and thus, a direct comparison cannot be made. However, from the Spotter wave spectra, we can estimate slope spectra as $k^2(f)S_\eta(f)$, where k is estimated from the linear dispersion relationship (A1) at each frequency at a depth of 10 m. In the swell band ($f < 0.1$ Hz), the plane-fit and 2D parabola-fit $S_{|\nabla\eta|}(f)$ for $R = 0.8$ m are elevated, indicating noise contamination. In this band the $S_{|\nabla\eta|}(f)$ converge with larger R (Fig. 7), suggesting that for $R \geq 1.2$ m the slope spectra are well estimated. In addition, in the swell band, the Spotter inferred $k^2S_\eta(f)$ (black dashed in Fig. 7) matches well the slope spectra for $R \geq 1.6$ m, further suggesting $S_{|\nabla\eta|}(f)$ is well estimated in this band. For $R \geq 1.6$ m, the equivalent swell-band wave slope $(ak)_{\text{swell}} = 0.0085$ (A2) is very small.

In the $0.1 < f < 0.4$ Hz sea band, the spectra are similar for both methods for all $R > 0.8$ m. Consistent with this, the equivalent sea-band wave slopes $(ak)_{\text{sea}}$ (A2) are similar in this band varying from 0.076 to 0.072. In addition, the inferred Spotter $k^2S_\eta(f)$ match well the slope spectra, which all together suggests that slope spectra are well estimated in this band. At higher frequencies ($f > 0.4$ Hz), the $S_{|\nabla\eta|}(f)$ separate as a function of R, are consistent with the reduced $\overline{|\nabla\eta|^2}$ with R (Fig. 5c) and the low-pass filter interpretation. Generally at $f > 2$ Hz for both methods, a noise floor is reached, whose level is lower for larger R, also consistent with the low-pass filter interpretation. For both methods, at $R = 0.8$ the $S_{|\nabla\eta|}(f)$ has a peak near $f = 0.6$ Hz which only weakly decays out to 1 Hz, whereas the slope spectra for larger R fall off much more rapidly. In the "chop" band ($0.4 < f < 1$ Hz) the equivalent ak is similar to that in the sea band, varying and varies from 0.1 to 0.05 for $R = 0.8$ m to $R = 2.4$ m, consistent with Fig. 7. The Spotter inferred slope spectra $k^2S_\eta(f)$ matches very well the $R = 0.8$ m 2D parabola-fit $S_{|\nabla\eta|}(f)$ in this band, suggesting that the slope of waves with wavelength as small as 1.6 m may be well estimated with the parabola fit. Similar to $\overline{|\nabla\eta|^2}$ and H_s^2(Fig. 5b,c), slope spectra $S_{|\nabla\eta|}(f)$ is more sensitive to R than $S_\eta(f)$ particularly at lower and higher frequencies.

5. Directional Fourier Coefficients, and Directional Moments

The results suggest that for $R \geq 1.2$ m, the slope spectra are well estimated at $f < 0.4$ Hz. However, wave-directional Fourier coefficients depend not only on the spectra of η, $\partial\eta/\partial x$, and $\partial\eta/\partial y$ but also on their cross-spectra (Longuet-Higgins et al. 1963). Here we estimate the directional Fourier coefficients ($a_1(f)$, $b_1(f)$, $a_2(f)$, $b_2(f)$) from the UAS-lidar derived spectra and cross-spectra using standard methods (Appendix) for $R \geq 1.2$ m and both fit methods (Fig. 8). The plane-fit

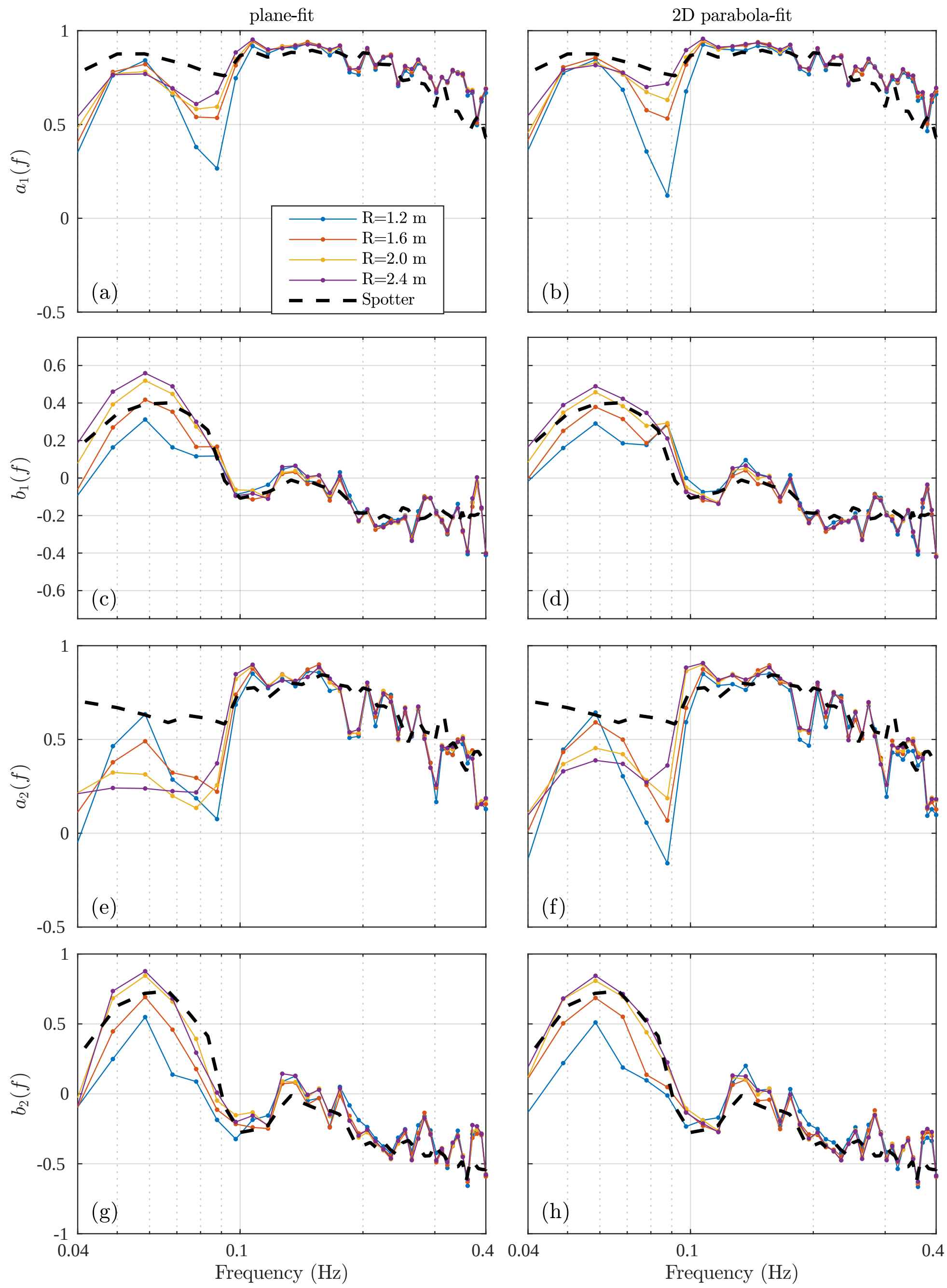

362 FIG. 8. Directional moments (a,b) $a_1(f)$, (c,d) $b_1(f)$, (e,f) $a_2(f)$, and (g,h) $b_2(f)$ versus frequency for (left-column) plane-fits and (right-column) 2D parabola-fits for five different sampling region radii of $R = \{1.2, 1.6, 2.0, 2.4\}$ m. The dashed line is the Spotter wave buoy derived directional moments. Note we limit comparison to 0.04–0.4 Hz.

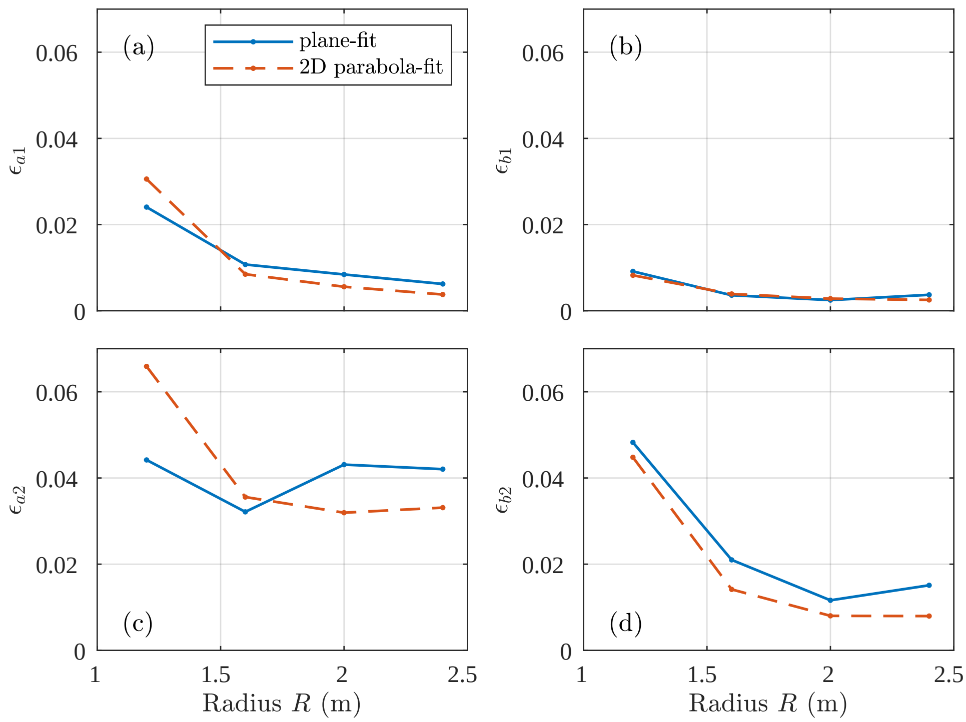

FIG. 9. Directional Fourier coefficient errors versus radius R for (a) ϵ_{a1}, (b) ϵ_{b1}, (c) ϵ_{a2}, and (d) ϵ_{b2} based on (7). The solid curve is from the plane-fit, and the dashed is from the 2D parabola-fit. The error metric (7) is integrated over the frequency band from 0.04 to 0.25 Hz containing the majority of wave energy and where the Spotter has been validated.

$a_1(f)$ follows the Spotter $a_1(f)$ for $R \geq 2$ m in the swell band ($0.04 < f < 0.1$ Hz). Most of the mismatch occurs near 0.08-0.09 Hz, where the S_η and slope spectra levels are reduced (Fig. 6, 7). The plane-fit $a_1(f)$ matches the Spotter $a_1(f)$ in the sea band ($0.1 < f < 0.4$ Hz) for all R (Fig. 8a). The 2D parabola-fit $a_1(f)$ is overall similar but is closer to the Spotter $a_1(f)$ in the swell band for the largest R (Fig. 8b). Overall, $b_1(f)$, $a_2(f)$, and $b_2(f)$ also agree well with the Spotter in the sea band ($0.1 < f < 0.4$ Hz) for the range of R (Fig. 8c–h) for both methods. For both methods, $b_1(f)$ and $b_2(f)$ match the Spotter's estimate in the swell band for larger R (Fig. 8c,d,g,h). In the sea band, $a_2(f)$ from both methods is similar to the Spotter (Fig. 8e,f). However, in the swell band, the comparison is poor. The Spotter $a_2(f)$ is quasi-constant in the swell band. For smaller R, the $a_2(f)$ for both methods varies strongly across the swell band, but becomes more constant at larger R, albeit at a lower value than the Spotter.

The preceding comparison between estimated directional Fourier coefficients and those of the Spotter are qualitative. Here, we make the comparison quantitative with an unweighted mean square error metric defined as,

$$\epsilon_{a1} = \left[\left(a_1(f) - a_1^{\mathrm{Sp}}(f) \right)^2 \right], \tag{7}$$

where the $[\ldots]$ represents an average over the frequency band 0.04–0.25 Hz and a_1^{Sp} is a_1 from the Spotter. This sea-swell frequency band contains the bulk of the wave energy (Fig. 6) and also is the range where the Spotter has been validated (Raghukumar et al. 2019). The errors for the other directional Fourier coefficients ϵ_{b1}, ϵ_{a2}, and ϵ_{b2} are similarly defined. These errors are estimated for both plane-fit and 2D parabola-fit methods. Consistent with Fig. 8a,b, the mean square error ϵ_{a1} decreases with increasing R with smallest error $\epsilon_{a1} \approx 0.005$ at $R = 2.4$ m (Fig. 9a), which is a small error relative to the $a_1(f)$ variability (Fig. 8a). The 2D parabola-fit method has slightly lower ϵ_{a1} than the plane-fit method. For $b_1(f)$, ϵ_{b1} is small for all R and largely decreases with R, and the 2D parabola-fit method is marginally better than the plane-fit (Fig. 9b). Consistent with Fig. 8e,f, the ϵ_{a2} has the largest error of all directional Fourier coefficients (Fig. 9c). For the 2D parabola-fit, ϵ_{a2} decreases or plateaus with R whereas the plane-fit ϵ_{a2} is not monotonic, and for $R \geq 2$ m is substantially larger than that of the plane-fit. For $b_2(f)$, the error ϵ_{b2} is large for small R and largely decreases with R (Fig. 9d). As with other directional Fourier coefficients, the 2D parabola-fit has smaller ϵ_{b2} than the plane-fit, and at $R = 2.4$ is at levels similar to ϵ_{a1}.

Accurately estimating directional Fourier coefficients is essential for any directional wave measurement, whether wave buoy or remote sensing. However, interpreting these directional Fourier coefficients can be opaque. For practical interpretation of directional wave properties, the directional Fourier coefficients are used to estimate directional moments such as the mean wave angle $\theta(f)$ and a directional spread $\sigma_\theta(f)$ at each frequency (Kuik et al. 1988, also see Appendix). Alternatively, they are used as inputs for directional spectra estimators such as MEM or IMLE (e.g., Oltman-Shay and Guza 1984). Mean wave direction has two definitions $\theta_1(f)$ (A7) and $\theta_2(f)$ (A8) which use (a_1, b_1) and (a_2, b_2), respectively (Kuik et al. 1988). The mean wave angle is defined as the direction of wave propagation in the China Rock coordinate system. Thus, onshore propagating waves with a component in the $+y$ direction have positive θ and with a component

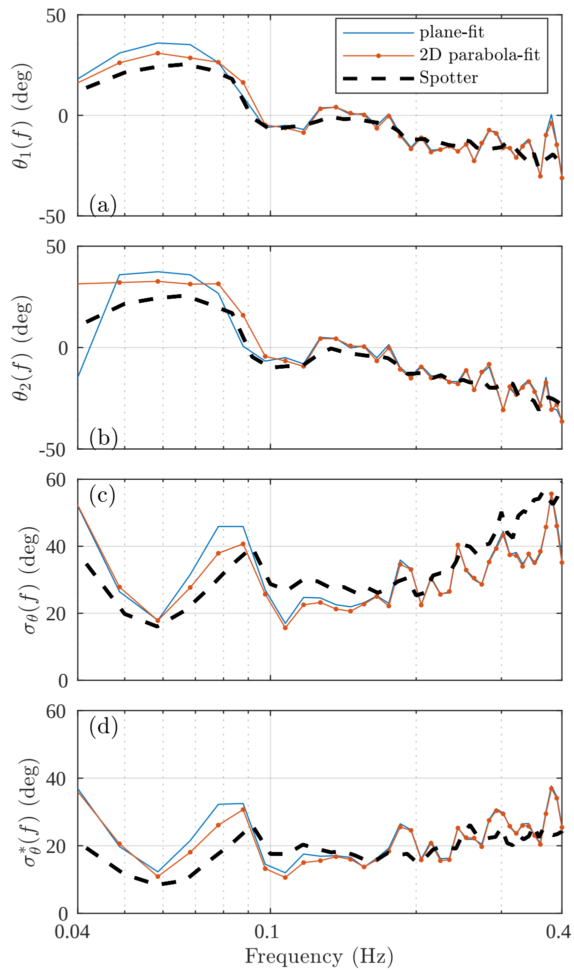

FIG. 10. Mean directions (a) θ_1 (A7) and (b) θ_2 (A8), and directional spreads (c) $\sigma_\theta(f)$ (A9), and (d) σ_θ^* (A10) versus frequency for the (blue) plane-fits, (orange) 2D parabola-fit, and (black) Spotter.

in the $-y$ direction have negative θ. Similarly, wave directional spread has two definitions (Kuik et al. 1988), the first $\sigma_\theta(f)$ (A9) utilizing (a_1, b_1) only, and $\sigma_\theta^*(f)$ utilizes all directional Fourier coefficients (A10).

For the two methods, the $\theta_1(f)$ varies from $\approx 25°$ to $0°$ in the swell band, and, in the sea-band, is largely negative and reducing with frequency. Using energy-weighted directional Fourier coefficients (Appendix), the swell-band $\bar{\theta}_{1,\text{swell}} = 28°$ and the sea-band $\bar{\theta}_{1,\text{sea}} = -9°$ for the 2D parabola-fit. The $\theta_1(f)$ from the two methods largely agrees well with the Spotter (Fig. 10a), consistent with the well estimated $a_1(f)$ and $b_1(f)$ (Figs. 8, 9). The agreement is quite good in the sea band where $\bar{\theta}_{1,\text{sea}} = -12°$. In the swell band, although the functional form is similar, the Spotter has consistently reduced wave angle relative to the two methods, with swell-band $\bar{\theta}_{1,\text{swell}} = 13°$. For both methods, $\theta_2(f)$ varies from 35° to 0° in the swell band and steadily decreases in the sea band similar to $\theta_1(f)$ (Fig. 10b). In the sea band, $\theta_2(f)$ for both methods are nearly identical and match well with the Spotter. In the swell band, $\theta_2(f)$ has a larger magnitude than that of the Spotter, with the 2D parabola-fit somewhat closer to the Spotter. Even with the relatively large ϵ_{a2} (Fig. 9c), the overall $\theta_2(f)$ compares well with the Spotter in the swell band.

The first directional spread estimator $\sigma_\theta(f)$ (A9) is $\approx 20°$ at the $f = 0.06$ Hz $S_\eta(f)$ peak and is larger $\approx 40°$ near $f = 0.085$ Hz where $S_\eta(f)$ is reduced (Fig. 10c). The 2D parabola-fit σ_θ is somewhat closer to that of the Spotter. In the sea band, the two estimators and the Spotter $\sigma_\theta(f)$ increase similarly with f, where the Spotter is generally larger than the two estimators. The second directional spread estimator $\sigma_\theta^*(f)$ (A10) is $\approx 12°$ at the $f = 0.06$ Hz $S_\eta(f)$ peak and is consistent with the Spotter $\sigma_\theta^* = 10°$ (Fig. 10d). At higher swell-band frequencies where the energy is low, $\sigma_\theta^*(f)$ increases like that of the Spotter. In the sea band, the estimated σ_θ^* generally increases from $\approx 13°$ at $f = 0.1$ Hz to $\approx 25°$ at $f = 0.4$ Hz with some fluctuations. In this band, the Spotter σ_θ^* has a similar pattern increasing from 17° to $\approx 25°$ with less fluctuations. Overall, both $\sigma_\theta(f)$ and $\sigma_\theta^*(f)$ compare well with the Spotter, particularly at frequencies where $S_\eta(f)$ is energetic, with the 2D parabola-fit performing slightly better. In sum, the results in Figs. 8 and 10 demonstrate the effectiveness of this method in estimating directional properties from a UAS with a mounted multi-beam scanning lidar.

6. Summary and Discussion

Previously, wave statistics seaward of the surf zone have not been estimated with a lidar due to lower number of returns, and directional wave moments have not been estimated with a lidar in any region. Here, we have developed and tested a method for estimating directional wave properties analogous to a wave buoy from a UAS with mounted multi-beam scanning lidar. The method was tested with an 11-minute hover at the location of a Spotter wave buoy on the rocky inner shelf in 10-m water depth offshore of the Monterey Peninsula. The UAS can effectively maintain a relatively fixed hover location. The method fits either a plane or a 2D parabola to lidar returns within a circular sampling region of varying radius R, resulting in estimates of the sea surface and its slope. Requiring at least $N_p = 10$ points within the sampling region leads us to consider radii with $R \geq 0.8$ m. Return and wave statistics are examined as a function of the radius of the sampling region and two methods. Results depend on R and weakly on the method.

Overall, the sea-surface elevation spectrum $S_\eta(f)$ comparison between the Spotter and the UAS-lidar is quite good for $R \geq 0.8$ m. This is similar to the accurate wave spectra estimated in the swash zone (Brodie et al. 2015) and across the surfzone (Fiedler et al. 2021). However, our observations are on the inner shelf, seaward of the surfzone, where the lack of foam reduces the number of returns. In addition, the water was unturbid and had a diver-reported visibility of 6 m. Unturbid water also inhibits lidar returns. That $S_\eta(f)$ was so well estimated suggests that this methodology can also be applied to other ocean regions where waves are not breaking.

The convergence of the slope spectra $S_{|\nabla\eta|}(f)$ at larger R and the good comparison with an inferred slope from the Spotter wave buoy indicates that the wave slope is well estimated in the swell band for $R \geq 1.6$ m and in the sea band for all R. Overall, the slope spectra $S_{|\nabla\eta|}(f)$ are more sensitive to R than $S_\eta(f)$ particularly at the lower and higher frequencies. For $R \geq 1.6$ m, the swell-band equivalent wave slope $(ak)_{\text{swell}} = 0.0085$ (A2) is very small. This demonstrates the challenge of estimating slope in the swell band and also speaks to the accuracy of the georeferenced lidar data and the ability of the method to accurately fit slopes for larger radii. The swell-band (0.04-0.1 Hz) waves have wavelength varying from 245 to 96 m. For normally-incident waves, the array width $2R$ is < 5 m, indicating that swell-band wave slope can still be accurately estimated with such a small array width. At a particular frequency, wavelengths are longer in deep water, so larger radii may be needed in the swell band. This may potentially bias directional estimates due to the lidar beam distribution. The sea-band wave slope $(ak)_{\text{sea}} \approx 0.075$ is an order of magnitude larger than that of the swell band and is similar for all R, suggesting that it is well estimated in this band. The relatively small $(ak)_{\text{sea}}$ also suggests nonlinearities are weak in this band. In the sea band, the ratio $2R/\lambda$ is always < 0.5 indicating that the wave slope should not be aliased. In the "chop" band frequencies (0.4–1 Hz), the $R = 0.8$ m 2D parabola-fit matches well the wave-buoy inferred slope (Fig. 7b), whereas wave slopes for larger R are reduced substantially due to the low-pass filter effect (or aliasing). Although this comparison is indirect, it suggests that the high-frequency fluctuations in the η and $\partial\eta/\partial x$ timeseries for $R = 0.8$ m (Fig. 4) are real and not noise. If the wave-buoy-derived slope is accurate in the "chop" band, this suggests that the georeferenced lidar data and this methodology may be useful in inferring wave properties also in the chop band.

Directional Fourier coefficients are computed from $S_\eta(f)$, the individual components of slope spectra, and their cross-spectra. All four coefficients compared well to the Spotter in the sea band, and only $a_2(f)$ did not perform well in the swell band. This is likely due to the functional form of $a_2(f)$ which depends on the difference in the x and y slope spectra $S_{\eta_x}(f) - S_{\eta_y}(f)$ (A5). In the swell band, slopes are very small, and thus the noise floor is likely elevated, which when subtracted (A5) could bias low $a_2(f)$ in the swell band. From 0.04-0.25 Hz, the 2D-parabola fit at the largest $R = 2.4$ m gave the best results. In the sea band, the comparison of directional moments (Fig. 10) was quite good. In the swell band, the magnitude of the mean wave angle and the directional spreads were larger than that of the Spotter.

In the discussion between UAS-lidar derived and Spotter quantities, we have not explicitly considered the errors of the Spotter wave buoy. The Spotter wave buoy has only been compared to Datawell wave buoys across from 0.05-0.3 Hz (Raghukumar et al. 2019), although we show Spotter wave buoy results out to 1 Hz. Thus, any conclusions based on comparison with Spotter between 0.3 Hz and 1 Hz are tentative. The differences in wave spectra between Spotter and Datawell Waverider buoys (Raghukumar et al. 2019) are consistent with the differences observed here (Fig. 6). Mean wave direction (energy weighted from 0.05-0.3 Hz) have rms differences to a Waverider buoy of $\approx 5°$, consistent with the differences observed here in the sea band. More recently, wave buoys were compared to a fixed pressure sensor array over a 3 month period (Collins et al. 2023). This comparison was performed across a low-frequency (0.035-0.065 Hz), a mid band (0.065–0.165 Hz) and a high band (0.165-0.26 Hz). Overall, the Spotter wave height and wave direction compared well to that of the pressure sensor array in the mid to high-frequency bands. This is consistent with our good comparison in the sea band. However, in the low-frequency band the Spotter wave buoy had significant differences in wave height and wave angles. In particular root-mean-square wave angle errors were $8°$, which is consistent with the wave angle differences between the UAS-lidar and Spotter (Fig. 10a,b). Another consideration is that we have performed a single comparison utilizing 11 min of UAS-lidar observations that overlapped within one hour of Spotter observations. An evolving wave field over this hour would also lead to differences in wave statistics. Overall, the internal consistency of the UAS-lidar-derived results and their good comparison to the Spotter wave buoy demonstrate that this is an effective tool for estimating wave statistics, particularly in regions near cliffs and rocky coasts.

Acknowledgments. This paper is part of the ROcky Shore: eXperiment and SImulations (ROXSI) project, funded by the Office of Naval Research through grants N000142112786 and N0001423WX01357. The Monterey NOAA Sanctuary, CA Fish and Wildlife, and Pebble Beach provided environmental permission for the experiment with permitting support provided by Chris Miller. We thank the SIO and NPS field crews for their invaluable support with the field experiment; for SIO: Brian Woodward, Kent Smith, Rob Grenzeback, Lucian Parry, Shane Finnerty, Carson Black, Duncan Wheeler, Annie Adelson, Loren Clark, Kaden Quinn, and Kanoa Pick; for NPS: Paul Jessen, Charlotte Benbow, Pat Collins, Mike Cook, Matt Gough, and Ian Jenstrom. We appreciate the valuable discussions with the ROXSI team that informed this manuscript. Julia Fiedler and Alex Simpson provided valuable comments and feedback on the manuscript.

Data availability statement. The data presented in this paper will be made available at the Zenodo.org data repository.

APPENDIX

A1. Dispersion Relationship, Directional Fourier Coefficients, and Directional Moments

For reference, the linear dispersion relationship for surface gravity waves is

$$\omega = \sqrt{gk \tanh(kh)} \tag{A1}$$

where $\omega = 2\pi f$ is the wave radian frequency, g is gravity, k is the wavenumber, and h is the still water depth. In wave theory, the monochromatic wave slope ak is a standard measure of wave nonlinearity. From the slope spectra, an equivalent swell- and sea-band ak is calculated as

$$(ak)_{\text{swell}} = \sqrt{2 \int_{\text{swell}} S_{|\nabla\eta|} \, \mathrm{d}f} \tag{A2}$$

where the swell band is $0.04 \leq f < 0.1$ Hz. Similarly, $(ak)_{\text{sea}}$ is defined over the $0.1 \leq f < 0.4$ Hz band and $(ak)_{\text{chop}}$ is defined over the $0.4 \leq f < 1$ Hz band.

We define the directional moments used to calculate the mean wave angle $\theta(f)$ and directional spread $\sigma_\theta(f)$. As in the text, sea-surface elevation spectra are given by $S_\eta(f)$ and cross-shore and alongshore slope spectra are given by $S_{\eta_x}(f)$ and $S_{\eta_y}(f)$, respectively. The co-spectrum (real part of the cross-spectrum) between η_x and η_y is given by $C_{\eta_x\eta_y}(f)$. The quad-spectrum (imaginary part of the cross-spectrum) between η and η_x is defined as $Q_{\eta\eta_x}(f)$ and similarly between η and η_y. With these definitions the directional moments are (e.g., Longuet-Higgins et al. 1963; Kuik et al. 1988; Herbers et al. 1999),

$$a_1(f) = \frac{\int_{-\pi}^{\pi}\cos(\theta)E(f,\theta)\mathrm{d}\theta}{\int_{-\pi}^{\pi}E(f,\theta)\mathrm{d}\theta} = \frac{-Q_{\eta\eta_x}(f)}{[S_\eta(f)(S_{\eta_x}(f)+S_{\eta_y}(f))]^{1/2}}, \tag{A3}$$

$$b_1(f) = \frac{\int_{-\pi}^{\pi}\sin(\theta)E(f,\theta)\mathrm{d}\theta}{\int_{-\pi}^{\pi}E(f,\theta)\mathrm{d}\theta} = \frac{-Q_{\eta\eta_y}(f)}{[S_\eta(f)(S_{\eta_x}(f)+S_{\eta_y}(f))]^{1/2}}, \tag{A4}$$

$$a_2(f) = \frac{\int_{-\pi}^{\pi}\cos(2\theta)E(f,\theta)\mathrm{d}\theta}{\int_{-\pi}^{\pi}E(f,\theta)\mathrm{d}\theta} = \frac{S_{\eta_x}(f)-S_{\eta_y}(f)}{S_{\eta_x}(f)+S_{\eta_y}(f)}, \tag{A5}$$

$$b_2(f) = \frac{\int_{-\pi}^{\pi}\sin(2\theta)E(f,\theta)\mathrm{d}\theta}{\int_{-\pi}^{\pi}E(f,\theta)\mathrm{d}\theta} = \frac{2C_{\eta_x\eta_y}(f)}{S_{\eta_x}(f)+S_{\eta_y}(f)}. \tag{A6}$$

The directional moments, such as mean wave angle and directional spread are functions of the Fourier coefficients (e.g., Kuik et al. 1988)

$$\theta_1(f) = \tan^{-1}\left(\frac{b_1(f)}{a_1(f)}\right), \tag{A7}$$

$$\theta_2(f) = 0.5\tan^{-1}\left(\frac{b_2(f)}{a_2(f)}\right), \tag{A8}$$

$$\sigma_\theta(f) = \sqrt{2[1-a_1(f)\cos(\theta_1(f))-b_1(f)\sin(\theta_1(f))]}, \tag{A9}$$

$$\sigma_\theta^*(f) = \sqrt{0.5[1-a_2(f)\cos(2\theta_1(f))-b_2(f)\sin(2\theta_1(f))]}, \tag{A10}$$

These directional moments are in radians and converted to degrees. We also estimate the mean wave angle averaged over the sea and swell band from energy-weighted directional Fourier coefficients, i.e., for the swell-band $\bar{a}_{1,\mathrm{swell}}$,

$$\bar{a}_{1,\mathrm{swell}} = \frac{\int_{\mathrm{swell}} a_1(f)S(f)\,\mathrm{d}f}{\int_{\mathrm{swell}} S(f)\,\mathrm{d}f} \tag{A11}$$

and similarly for the other Fourier coefficients. The mean wave angle in the swell (or sea) band is then defined as

$$\bar{\theta}_{1,\text{swell}} = \tan^{-1}\left(\frac{\bar{b}_{1,\text{swell}}}{\bar{a}_{1,\text{swell}}}\right). \tag{A12}$$

References

Almeida, L. P., G. Masselink, P. Russell, M. Davidson, T. Poate, R. McCall, C. Blenkinsopp, and I. Turner, 2013: Observations of the swash zone on a gravel beach during a storm using a laser-scanner (lidar). *Journal of Coastal Research*, 636–641.

Baker, C. M., M. Moulton, M. L. Palmsten, K. Brodie, E. Nuss, and C. C. Chickadel, 2023: Remotely sensed short-crested breaking waves in a laboratory directional wave basin. *Coastal Engineering*, **183**, 104 327, https://doi.org/https://doi.org/10.1016/j.coastaleng.2023.104327, URL https://www.sciencedirect.com/science/article/pii/S0378383923000510.

Blenkinsopp, C., M. Mole, I. Turner, and W. Peirson, 2010: Measurements of the time-varying free-surface profile across the swash zone obtained using an industrial lidar. *Coastal Engineering*, **57 (11)**, 1059–1065, https://doi.org/https://doi.org/10.1016/j.coastaleng.2010.07.001.

Blenkinsopp, C. E., I. L. Turner, M. J. Allis, W. L. Peirson, and L. E. Garden, 2012: Application of lidar technology for measurement of time-varying free-surface profiles in a laboratory wave flume. *Coastal Engineering*, **68**, 1–5, https://doi.org/https://doi.org/10.1016/j.coastaleng.2012.04.006.

Brodie, K. L., B. L. Bruder, R. K. Slocum, and N. J. Spore, 2019: Simultaneous mapping of coastal topography and bathymetry from a lightweight multicamera uas. *IEEE Transactions on Geoscience and Remote Sensing*, **57 (9)**, 6844–6864, https://doi.org/10.1109/TGRS.2019.2909026.

Brodie, K. L., B. Raubenheimer, S. Elgar, R. K. Slocum, and J. E. McNinch, 2015: Lidar and pressure measurements of inner-surfzone waves and setup. *Journal of Atmospheric and Oceanic Technology*, **32 (10)**, 1945 – 1959, https://doi.org/10.1175/JTECH-D-14-00222.1.

Collins, C. O., P. Dickhudt, J. Thomson, E. Terrill, and L. Centurioni, 2023: Performance of moored gps wave buoys. *Coastal Engineering Journal*, submitted.

Feddersen, F., A. Amador, K. Pick, A. Vizuet, K. Quinn, E. Wolfinger, J. H. MacMahan, and A. Fincham, 2023a: The wavedrifter: a low-cost imu-based lagrangian drifter to observe steepening and overturning of surface gravity waves and the transition to turbulence. *Coastal Engineering Journal*, **0 (0)**, 1–14, https://doi.org/10.1080/21664250.2023.2238949.

Feddersen, F., A. M. Fincham, K. L. Brodie, A. D. Young, M. S. Spydell, D. J. Grimes, M. Pieska, and K. Hanson, 2023b: Cross-shore wind-induced changes to field-scale overturning wave shape. *J. Fluid Mech.*, https://doi.org/10.1017/jfm.2023.40.

Fiedler, J. W., K. L. Brodie, J. E. McNinch, and R. T. Guza, 2015: Observations of runup and energy flux on a low-slope beach with high-energy, long-period ocean swell. *Geophysical Research Letters*, **42 (22)**, 9933–9941, https://doi.org/https://doi.org/10.1002/2015GL066124, https://agupubs.onlinelibrary.wiley.com/doi/pdf/10.1002/2015GL066124.

Fiedler, J. W., L. Kim, R. L. Grenzeback, A. P. Young, and M. A. Merrifield, 2021: Enhanced surf zone and wave runup observations with hovering drone-mounted lidar. *Journal of Atmospheric and Oceanic Technology*, **38 (11)**, 1967 – 1978, https://doi.org/10.1175/JTECH-D-21-0027.1.

Herbers, T., S. Elgar, and R. T. Guza, 1999: Directional spreading of waves in the nearshore. *Journal of Geophysical Research-Oceans*, **104**, 7683–7693, https://doi.org/10.1029/1998JC900092.

Herbers, T., P. Jessen, T. Janssen, D. Colbert, and J. MacMahan, 2012: Observing ocean surface waves with gps-tracked buoys. *Journal of Atmospheric and Oceanic Technology*, **29 (7)**, 944–959.

Herbers, T. H. C., and S. J. Lentz, 2010: Observing directional properties of ocean swell with an acoustic doppler current profiler (adcp). *Journal of Atmospheric and Oceanic Technology*, **27 (1)**, 210 – 225, https://doi.org/https://doi.org/10.1175/2009JTECHO681.1.

Huang, Z.-C., C.-Y. Yeh, K.-H. Tseng, and W.-Y. Hsu, 2018: A uav–rtk lidar system for wave and tide measurements in coastal zones. *Journal of Atmospheric and Oceanic Technology*, **35 (8)**, 1557 – 1570, https://doi.org/https://doi.org/10.1175/JTECH-D-17-0199.1, URL https://journals.ametsoc.org/view/journals/atot/35/8/jtech-d-17-0199.1.xml.

Hwang, P. A., D. W. Wang, E. J. Walsh, W. B. Krabill, and R. N. Swift, 2000: Airborne measurements of the wavenumber spectra of ocean surface waves. part i: Spectral slope and dimensionless spectral coefficient. *Journal of Physical Oceanography*, **30 (11)**, 2753 – 2767, https://doi.org/https://doi.org/10.1175/1520-0485(2001)031⟨2753:AMOTWS⟩2.0.CO;2.

Irish, J. L., J. M. Wozencraft, A. G. Cunningham, and C. Giroud, 2006: Nonintrusive measurement of ocean waves: Lidar wave gauge. *J. Atmos. Oceanic Technol.*, **23**, 1559–1572.

Kuik, A. J., G. P. Van Vledder, and L. H. Holthuijsen, 1988: A method for the routine analysis of pitch-and-roll buoy wave data. *Journal of Physical Oceanography*, **18 (7)**, 1020–1034, https://doi.org/10.1175/1520-0485(1988)018.

Lange, A. M., J. W. Fiedler, M. A. Merrifield, and R. Guza, 2023: Video-based estimates of nearshore bathymetry. *Coastal Engineering*, revised.

Lenain, L., and W. K. Melville, 2017: Measurements of the directional spectrum across the equilibrium saturation ranges of wind-generated surface waves. *Journal of Physical Oceanography*, **47 (8)**, 2123 – 2138, https://doi.org/https://doi.org/10.1175/JPO-D-17-0017.1, URL https://journals.ametsoc.org/view/journals/phoc/47/8/jpo-d-17-0017.1.xml.

Longuet-Higgins, M., D. Cartwright, and N. Smith, 1963: *Ocean Wave Spectra*, chap. Observations of the Directional Spectrum of Sea Waves Using the Motions of a Floating Buoy, 111–136. Prentice Hall.

Marques, O. B., J. H. MacMahan, and F. Feddersen, 2023: Estimating wave statistics from pressure sensors over complex topography. *J. Atmos. Oceanic Technol.*, in prep.

Martins, K., C. E. Blenkinsopp, H. E. Power, B. Bruder, J. A. Puleo, and E. W. Bergsma, 2017: High-resolution monitoring of wave transformation in the surf zone using a lidar scanner array. *Coastal Engineering*, **128**, 37–43, https://doi.org/10.1016/j.coastaleng.2017.07.007.

Melville, W. K., L. Lenain, D. R. Cayan, M. Kahru, J. P. Kleissl, P. F. Linden, and N. M. Statom, 2016: The modular aerial sensing system. *Journal of Atmospheric and Oceanic Technology*, **33 (6)**, 1169 – 1184, https://doi.org/10.1175/JTECH-D-15-0067.1.

O'Dea, A., K. Brodie, and S. Elgar, 2021: Field observations of the evolution of plunging-wave shapes. *Geophysical Research Letters*, **48 (16)**, e2021GL093 664, https://doi.org/https://doi.org/10.1029/2021GL093664.

Oltman-Shay, J., and R. T. Guza, 1984: A data-adaptive ocean wave directional-spectrum estimator for pitch and roll type measurements. *Journal of Physical Oceanography*, **14 (11)**, 1800 – 1810, https://doi.org/https://doi.org/10.1175/1520-0485(1984)014⟨1800:ADAOWD⟩2.0.CO;2.

Rabault, J., and Coauthors, 2022: Openmetbuoy-v2021: An easy-to-build, affordable, customizable, open-source instrument for oceanographic measurements of drift and waves in sea ice and the open ocean. *Geosciences*, **12 (3)**, 110.

Raghukumar, K., G. Chang, F. Spada, C. Jones, T. Janssen, and A. Gans, 2019: Performance characteristics of "spotter," a newly developed real-time wave measurement buoy. *Journal of Atmospheric and Oceanic Technology*, **36 (6)**, 1127 – 1141, https://doi.org/10.1175/JTECH-D-18-0151.1.

Turner, I. L., M. D. Harley, and C. D. Drummond, 2016: Uavs for coastal surveying. *Coastal Engineering*, **114**, 19–24, https://doi.org/https://doi.org/10.1016/j.coastaleng.2016.03.011, URL https://www.sciencedirect.com/science/article/pii/S0378383916300370.

Wojtanowski, J., M. Zygmunt, M. Kaszczuk, Z. Mierczyk, and M. Muzal, 2014: Comparison of 905 nm and 1550 nm semiconductor laser rangefinders' performance deterioration due to adverse environmental conditions. *Opto-Electronics Review*, **22 (3)**, 183–190, https://doi.org/doi:10.2478/s11772-014-0190-2.